Wide band gap $Cu_2ZnGe(S,Se)_4$ thin films and solar cells: influence of Na content and incorporation method.

Andrea Ruiz-Perona[a,*], Maxim Guc[b], Yudania Sánchez[b], Tim Kodalle[c,1], José M. Merino[a], Máximo León[a], Raquel Caballero[a,*].

[a]Universidad Autónoma de Madrid, Departamento de Física Aplicada, C/ Tomás y Valiente 7, 28049 Madrid, Spain

[b]IREC, Catalonia Institute for Energy Research, C/ Jardins de les Dones de Negre 1, Sant Adriá del Besòs, 08930 Barcelona, Spain

[c]PVcomB, Helmholtz Zentrum Berlin für Materialien und Energie, Schwarzschildstrasse 3, Berlin 12489 Germany

* Corresponding authors: andrea.ruizp@estudiante.uam.es (Andrea Ruiz-Perona), raquel.caballero@uam.es (Dr. Raquel Caballero)

[1] Present Address: Molecular Foundry, Lawrence Berkeley National Laboratory, 1 Cyclotron Road, Berkeley CA 94720, USA.

ABSTRACT

The influence of the Na content and incorporation procedure into $Cu_2ZnGe(S,Se)_4$ (CZGSSe) thin films and solar cells is investigated. The effects of the presence/absence of Se during the deposition of a 15 nm thick NaF layer before and/or after the $Cu_2ZnGeSe_4$ (CZGSe) co-evaporation, are compared. Both the Na content, and Na-supply method significantly influence the incorporation of S into the CZGSe lattice and its distribution in the absorber. A [S]/([S]+[Se])-gradient throughout the CZGSSe layers is observed for all the samples and correlated with effects induced by the Na incorporation procedure. For instance, the evaporation of Se together with NaF leads to an increased S concentration in the surface-region of the CZGSSe layer and a modified surface

morphology. CZGSSe-based solar cells with band gap energies of about 2 eV are obtained, regardless of the NaF addition method used, while the absence of the NaF layer reduces the S incorporation and the E_g. However, the evaporation of Se together with NaF results in higher E_g and open circuit voltage V_{OC}, probably related to a higher S accumulation near the surface, demonstrating the importance of the [S]/([S]+[Se]) distribution. CZGSSe-based photovoltaic devices with efficiency of 3.2 % and E_g of 2 eV are obtained.
Keywords: $Cu_2ZnGe(S,Se)_4$; sulfurization; Na; Se; wide band gap; solar cells

1. Introduction

Wide band gap absorber materials are very attractive candidates for photovoltaic devices because they open up new market opportunities and increase the range of applications. In particular, they have potential to tackle two main technological applications. Firstly, they can be used as top cells in cost-efficient tandem devices. For that, absorbers with band gap energy E_g in the range of 1.5-1.9 eV are necessary (Bremner et al. 2008, Honsberg and Bowden 2020). Secondly, absorbers with $E_g \geq 1.5$ eV can be used in semi-transparent devices for efficient and stable Building Integrated Photovoltaic (BIPV) concepts. The (semi)-transparent solar cells that have produced the most promising results so far, are those based on perovskite (Rahmany and Etgar, 2020) and organic materials; however, they have not demonstrated sufficient stability yet. Thin-film inorganic solar cells are a great alternative, presenting the advantage of having high efficiency, flexibility, stability and low cost. Up to date, the most efficient thin-film photovoltaic devices are CdTe and $CuIn_{1-x}Ga_xSe_2$ (CIGSe) compounds with conversion efficiencies up to 22.1 % (Green et al. 2019) and 23.3 % (Nakamura et al. 2019) respectively. However, they require scarce or toxic elements as In, Ga, Cd and Te for their fabrication, which complicates large scale production. Kesterite $Cu_2ZnSn(S_xSe_{1-x})_4$ (CZTSSe) appears as an alternative to CIGSe by substituting In and Ga for earth-abundant elements such as Zn and Sn. Nevertheless, the

highest efficiency achieved by a kesterite-based solar cell up to now is 12.6% (Son et al. 2019, Wang et al. 2014), and one of the main limiting factors of this technology is the low open-circuit voltage (V_{OC}). The reasons for this are still under research, but the most likely explanations might be the presence of structural defects, secondary phases formation or a short carrier lifetime (Giraldo et al. 2019).

Kesterite materials present a direct and tunable band gap energy, which can be modified by substituting Se atoms with S. In the past few years, substitution of Sn with Ge has come out as an alternative to further increase the bandgap energy (Ford et al. 2011, Guo et al. 2012). The E_g varies with the [Ge]/([Sn]+[Ge]) (x) atomic ratio, and ranges from 1.0 eV for $Cu_2ZnSnSe_4$ (CZTSe, $x = 0$) compounds up to 1.4 eV for $Cu_2ZnGeSe_4$ (CZGSe, $x = 1$) materials (Kim et al. 2016). In recent studies, CZGSe-based photovoltaic devices with E_g = 1.4 eV and 8.5 % efficiency, with an improved V_{OC} have been achieved (Choubrac et al. 2020), showing the effectivity of Ge incorporation into the kesterite. For materials with $x = 1$, by increasing the [S]/([S]+[Se]) atomic ratio, band gap energy raises from 1.4 eV in CZGSe up to 2.2 eV in Cu_2ZnGeS_4 (CZGS) compounds (Garcia-Llamas et al. 2016). However, it has been observed that the V_{OC} deficit, $E_g/q - V_{OC}$, increases with E_g (Guo et al. 2012). Therefore, fabricating wide band gap kesterite solar cells while keeping high efficiencies is a challenge. In order to improve the device performance, it is necessary to optimize the sulphur content and its distribution through the absorber layer, both of which strongly affect the properties of the material. Kohl et al. (2018) observed an inhomogeneous distribution of the [S]/([S] + [Se]) atomic ratio through the CZGSSe kesterite layer when metallic precursors were annealed with H_2Se and H_2S, detecting a sulphur inclusion at the surface up to 20 % higher than in the bulk material. It has been observed in literature that sulfurization of the surface of the absorber leads to a higher E_g on the surface, increasing the V_{OC} and device efficiency (Cai et al. 2017). Schnabel et al.

(2017a, 2017b) controlled the [S]/([S] + [Se]) atomic ratio via addition of variable amounts of GeS during the annealing of kesterite deposited by chemical solution, obtaining CZGSSe-based solar cells with E_g = 1.54 eV and 1.47 eV as well as η = 2.1 % and 6.0 % respectively. By improving the absorber band gaps and the device efficiencies, wide band gap kesterite materials could be considered a potential candidate to use as top cell absorber in tandem devices (Khelifi et al. 2021, Vermang et al. 2019) or in BIPV applications as semi-transparent solar cells (Becerril-Romero et al. 2020).

An improvement in V_{OC} -deficit has been achieved by addition of alkali metals, out of which Na is the most studied element. Previous reports have observed that Na incorporation has, in general, a beneficial effect on both the properties of the kesterite absorbers and the complete devices. Effects include larger grain size and suppression of Sn_{Cu} and Ge_{Cu} point defects which are detrimental for the device performance (Neuschitzer et al. 2018). It has also been observed that Na addition into the kesterite absorbers increases the charge carrier concentration and shifts the Fermi level towards the valence band maximum (Li et al. 2013), which increases V_{OC}. Nevertheless, a reduction of the depletion width in Na-containing samples has been observed, which decreases J_{SC} (Li et al. 2013). In order to describe the effect of sodium on kesterite solar cells, different explanations have been proposed. One possibility is that Na tends to occupy Cu sites in the kesterite lattice, preventing the formation of other substitutional defects on Cu positions. Another explanation could be that during the kesterite synthesis at high temperature, Na occupies Cu positions, but during the cooling stage, the Na diffuses towards the grain boundaries, leaving a high amount of Cu vacancies, which would increase the *p*-type conductivity of the material (Giraldo et al. 2019).

Some years ago, it was observed that the method of addition of the alkali elemental has a significant influence on the performance of CIGSe-based solar cells (Caballero et al.

2011). World record efficiency of CIGSe photovoltaic devices on flexible substrates was achieved when a NaF layer was supplied by a post-deposition treatment (PDT) deposited after the CIGSe co-evaporation (Chirilá et al. 2011). Chang et al. (2021) have reported an improved CZTSSe device performance from 10.1 % to 11.7 % by the addition of a NaF layer added by a PDT process. They observed that Na atoms are randomly dispersed in both the grain interior and grain boundaries, increasing the acceptor concentration and passivating the deep level defects to enhance the V_{OC}. More recently, we have investigated the effect of a NaF precursor layer on the properties of CZGSSe thin films, achieving an efficiency of 2.7 %, V_{OC} = 828 mV and E_g = 2 eV by the addition of 15 nm NaF precursor layer (Ruiz-Perona et al. 2021). For that, the absorber layer was deposited by the sulfurization of co-evaporated CZGSe layers. Here, different procedures to add Na in wide band gap kesterite material are compared.

In the present work, the effect of Na content and method of incorporation on the elemental distribution, composition as well as structural, vibrational and morphological properties of wide band gap kesterite thin films has been studied. For that, different $Cu_2ZnGe(S_xSe_{1-x})_4$ (CZGSSe) samples have been fabricated under the same growing conditions, only varying the NaF layer deposition procedure. The incorporation of S into the CZGSe lattice has been investigated, producing absorber layers with E_g in the range of 2.0 eV. Finally, complete photovoltaic devices have been fabricated and characterized. Up to our knowledge, it is the first time that an efficiency of 3.2 % is achieved for CZGSSe-based solar cells with E_g around 2 eV. This work reflects a first step to consolidate wide band gap kesterite materials, that could increase the range of applications.

2. Materials and methods

2.1 $Cu_2ZnGe(S,Se)_4$ thin films and photovoltaic devices fabrication

$Cu_2ZnGeSe_4$ thin films were fabricated by co-evaporation of Cu, ZnSe, Ge and Se onto Mo/soda-lime glass (SLG) substrates at a nominal substrate temperature of 150 ºC (Ruiz-Perona et al. 2021). This low temperature was chosen to reduce the re-evaporation of Ge and Se. Before the co-evaporation process, only Se was deposited for 3 min onto the Mo. The following CZGSe co-evaporation process consisted of 3 stages. During the first stage, Cu, ZnSe, Ge and Se were evaporated in order to obtain a Cu-rich composition during this stage to assist the formation of kesterite-type crystals. In the second stage, ZnSe, Ge and Se were deposited to achieve a final Cu-poor composition, and, finally, in the third stage, Ge and Se were evaporated to avoid a Zn excess on the surface (Ruiz-Perona et al. 2020a). The effect of Na on the kesterite was studied by changing the NaF layer deposition conditions, while keeping the same conditions during the CZGSe co-evaporation process. A NaF layer of a total nominal thickness of 15 nm, as measured by quartz crystal microbalance, was deposited at a substrate temperature of around 30-40 ºC. Fig. 1 shows the different configurations of the NaF layers. For Sample A, a 15 nm thick NaF layer was evaporated after the co-evaporation process (PD-layer); in Sample B, a 7.5 nm thick layer was deposited onto the Mo substrate, before the co-evaporation process (pre-layer), and another 7.5 nm thick NaF layer was deposited onto the CZGSe layer (PD-layer). Sample C has the same structure as Sample A, but the NaF layer was evaporated in the presence of Se; and for Sample D, the same procedure as for Sample B was followed, but the NaF layers were also deposited along with Se (Ruiz-Perona 2020b). Moreover, it is important to note that Na can diffuse from the SLG substrate into the kesterite. However, the co-evaporation process was carried out at a nominal temperature of 150 ºC as mentioned above, so the diffusion process during the deposition is expected to be rather weak. A Reference CZGSe Sample without any NaF layer was evaporated following the

same co-evaporation parameters to investigate the effect of Na content on the properties of the absorber layer.

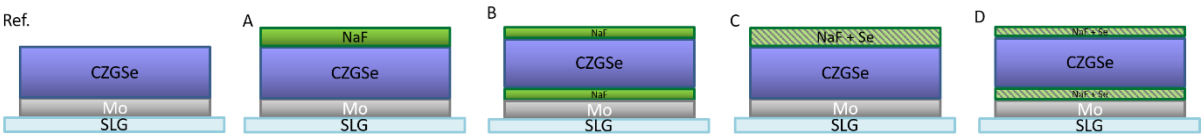

Fig. 1. Structure of Samples A-D and Reference before the sulfurization process. The layers thicknesses are not to scale.

The co-evaporation process was followed by a thermal treatment at 525 ºC in a tubular furnace in Ar atmosphere at a pressure of 930 mbar for one hour. The samples were placed into a graphite box, along with S and GeS in order to incorporate S into the material (Ruiz-Perona et al. 2021).

Complete photovoltaic devices with ITO/i-ZnO/CdS/CZGSSe/Mo/SLG structure were fabricated using these absorbers. A CdS buffer layer of 50 nm was deposited by chemical bath deposition, followed by 50 nm i-ZnO and a 350 nm of In_2O_3:SnO_2 (ITO) layers deposited by DC-pulsed sputtering to act as a transparent conductive window layer. The devices did not have antireflective coating nor metallic grids. The size of the cells was 3x3 mm^2.

2.2 Sample characterization

The chemical composition of the samples was measured by energy dispersive X-ray spectroscopy (EDX) using an Oxford INCAx-sight detector connected to a Hitachi S-3000N scanning electron microscope (SEM). Bulk measurements were carried out at 25 kV operating voltage, while surface composition was measured at 10 kV. Cu K, Zn K, Ge K, Se K and S K lines were used for elemental quantification. Glow discharge optical emission spectrometry (GD-OES) was used to measure the in-depth element distribution through the CZGSSe thin-film. The measurements were performed in a Spectruma GDA

650 spectrometer with Argon plasma in a pulsed RF mode for sputtering and a CCD-array for the optical detection. The measurements are shown in arbitrary units since they were performed without a calibration sample (Kodalle et al. 2019). Grazing incidence X-ray diffraction (GIXRD) was measured using a PANAlytical X'Pert Pro MPD diffractometer, with CuK_{α} radiation and a multilayer mirror to produce a parallel beam. The measurements were performed at incidence angles of 1º and 4º. The reference spectra for phase identification were taken from International Centre for Diffraction Data. The morphology of the CZGSSe/Mo structure and the CZGSSe surface was investigated by SEM using a SEM FEI VERIOS 460, operating at 2 kV. Raman scattering spectra were measured using two monochromators FHR 640 and iHR 320 from Horiba Jobin Yvon, both coupled with CCD detectors. The first monochromator is optimized for the UV and visible range and was used with gas (325 and 442 nm) and solid state (532 nm) lasers as excitation sources. The second monochromator is optimized to the NIR spectral range and was used with solid state (785 nm) laser as excitation source. The lasers power density was in the range of 100 W cm^{-2} – 150 W cm^{-2}. The spectra were measured in backscattering configuration using a special probe designed at IREC. Spectral position was corrected by imposing the main peak of single crystalline Si to 520 cm^{-1}.

Current-Voltage (*IV*) characterization was performed in a Sun 3000 class solar simulator (Abet Technologies Inc., Milford, Connecticut, USA) under AM1.5 and 100 mW cm^{-2} illumination conditions at 25 ºC. External quantum efficiency (*EQE*) was measured using a Bentham PVE300 system (Bentham Instruments Ltd., Berkshire, UK) calibrated with a Si and Ge photodiode and the spot size was almost 3x3 mm^2.

3. Results and discussion

The atomic composition of each sample measured by EDX is shown in Table 1. The measurements done at 25 kV show that the [Cu]/([Zn]+[Ge]) and [Zn]/[Ge] atomic ratios are comparable for all the samples with NaF, and the main difference is found in the [S]/([S]+[Se]) ratio, for the latter is decreased in Samples C and D, where NaF was deposited in the presence of Se. The Reference sample has a slightly higher Cu concentration and a much lower S content in the bulk of the kesterite layer. In agreement with our previous experiments (Ruiz-Perona et al. 2021), a higher incorporation of S into the bulk of CZGSe layers takes place by increasing the Na content. The surface-sensitive EDX-measurements performed at 10 kV show a higher S concentration and an increased [S]/([S]+[Se]) atomic ratio, which is more significant for Samples C, D and the Reference sample. Therefore, a non-uniform in-depth sulphur distribution is expected. A higher Cu-content is also observed at the surface of all the samples, which can be detrimental for the CdS/CZGSSe heterojunction. However, it is detected that the addition of Na via a NaF layer leads to a decreased Cu concentration in agreement with the known affinity of Na for the Cu vacancies, V_{Cu} (Caballero et al. 2013, Niles et al. 1999). In addition, the evaporation of Se together with NaF, Samples C and D, results in a lower Cu content in the bulk and close to the surface of the absorber layer.

Table 1. Composition of all the samples measured by EDX using different acceleration voltages.

Sample		Cu (at %)	Zn (at %)	Ge (at %)	S (at %)	Se (at %)	[Cu]/ [Zn]+[Ge])	[Zn]/ [Ge]	[S]/ ([S]+[Se])
Ref	25 kV	20.5	13.0	11.0	13.6	41.9	0.85	1.18	0.25
	10 kV	22.7	14.6	11.6	24.6	26.5	0.87	1.27	0.48
A	25 kV	19.2	13.1	12.3	35.1	20.4	0.76	1.06	0.63
	10 kV	22.5	12.8	12.6	36.3	15.7	0.89	1.02	0.70
B	25 kV	19.1	12.8	12.7	33.0	22.3	0.75	1.01	0.60
	10 kV	22.3	11.8	11.7	39.3	14.7	0.94	1.01	0.69
C	25 kV	17.6	12.3	12.7	23.4	34.0	0.71	0.97	0.41
	10 kV	21.3	13.3	14.0	33.4	18.0	0.78	0.97	0.65
D	25 kV	18.0	13.1	12.4	25.8	30.7	0.71	1.06	0.46
	10 kV	21.9	14.4	12.5	30.5	20.7	0.82	1.17	0.60

In order to prove the inhomogeneous distribution of S in-depth of the absorber layer, GD-OES measurements were performed (see Fig. 2). Samples A and B have a more uniform elemental distribution, while Samples C and D present greater differences between the composition at the surface and the bulk of the absorber layer. First of all, there is a higher S concentration at the surface for all the samples, however, its distribution changes largely depending on the Na content and whether the NaF incorporation was made in presence of Se or not. A much lower S-signal is detected inside the bulk of the absorber layer for the Reference sample in comparison to the other CZGSSe absorber layers, in agreement with EDX results and similar to the results shown in (Ruiz-Perona et al.2021). Samples C and D exhibit a noticeable S-gradient throughout the CZGSSe layer, with a much higher

S-content at the surface in agreement with the EDX measurements. Besides, Sample B presents a more pronounced S gradient than Sample A. As it has been previously mentioned, the S distribution in the bulk of the absorber strongly affects the properties of the kesterite, especially its band gap energy, consequently also affecting the photovoltaic parameters of the corresponding solar cells (Cai et al. 2017, de la Cueva et al. 2018, Giraldo et al. 2019). The presence of Se during the evaporation of the NaF layer reduces the S-incorporation into the bulk of the CZGSe layer, showing a lower [S]/([S]+[Se]) atomic ratio and a significant increase of S at the surface of the absorber. This is independent of whether only the NaF layer was evaporated after the co-evaporation process (PD-layer) or a 7.5 nm thick layer was deposited before the co-evaporation process (pre-layer), and another 7.5 nm thick NaF layer was deposited onto the CZGSe layer (PD-layer). In contrast, Samples A and B, where there was no Se evaporation along with the NaF deposition, have a more uniform sulphur distribution across the CZGSSe layer. The depth profiles also show that the Se and S distributions exhibit opposite tendencies, which confirms that the Se atoms substitute S atoms. On the other hand, it can also be observed that the Cu in-depth distribution depends on the presence of Se during the evaporation of NaF. For Samples A and B, there is a reduced Cu content at the surface, but it remains constant in the bulk of the absorber, whereas Samples C and D present a higher Cu content at the surface decreasing towards the Mo back contact. The reference sample is also characterized by a decrease of Cu concentration from the absorber surface towards the Mo layer. The Ge-signal generally increases towards the surface, and – in the case of Sample C – also near the Mo layer. A slightly lower Zn-GD-OES signal is detected near the back contact for all the samples. Finally, differences in the Na in-depth distribution can also be observed. While Samples A and B present a double gradient with high Na content at the surface and next to the Mo back contact, Samples C and D have a

much higher Na concentration on the surface than in the bulk and near the back contact, similar to the S distribution, which is in agreement with previous observations for CIGSe solar cells (Kronik et al. 1998) where Na tends to occupy Se vacancies, thus, Na concentration increases when Se content is lower. It is important to note that as opposed to Sample B, in Sample A the Na signal is stronger in the bulk of the CZGSSe layer. A much lower Na-signal near the surface and back contact is measured for the Reference sample because the only source of the alkali element is the SLG substrate. This shows that changes in the Na amount and during the NaF incorporation to the material strongly affect the elemental distribution, especially the distribution of Na, S, Se, and Cu.

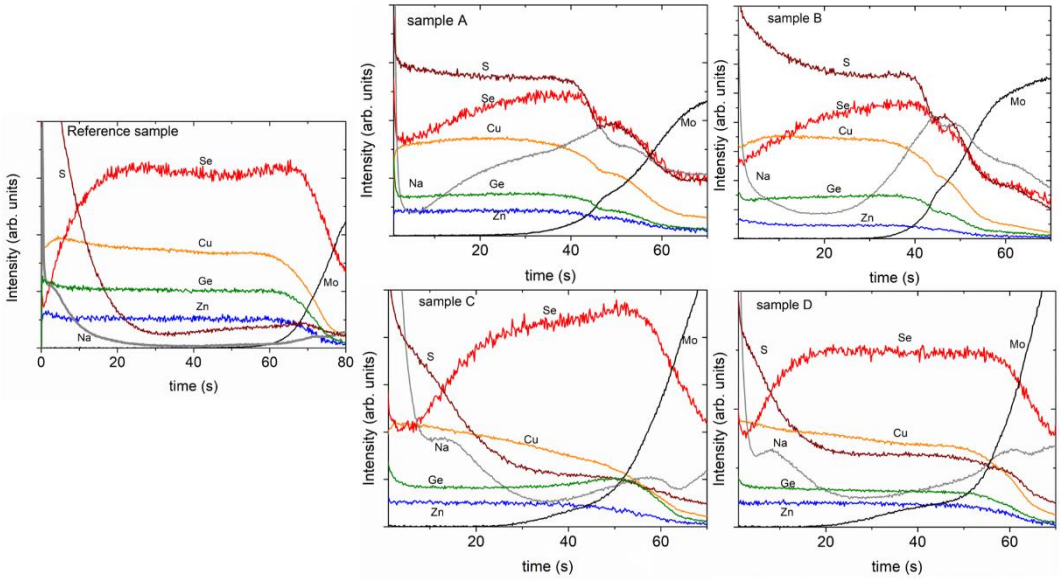

Fig. 2. GD-OES depth profiles of CZGSSe/Mo structure for all the samples.

Fig. 3 shows the in-depth profile of the normalized [S]/([S]+[Se]) atomic ratio for all the samples. Recently, we also observed a single [S]/([S]+[Se])-gradient through CZGSSe thin films with a NaF precursor layer of different thicknesses with a higher ratio at the surface and decreasing towards the back contact (Ruiz-Perona et al. 2021). As mentioned above, the Reference sample presents a much lower [S]/([S]+[Se]) atomic ratio inside the absorber layer in comparison with the other samples, and a pronounced increase towards

the surface, in agreement with EDX measurements. While in Samples A and B the [S]/([S]+[Se]) ratio is more uniform, only slightly decreasing towards the Mo contact, in Samples C and D, there is a great difference between the surface and the bulk of the absorber layer, being more significant for Sample C. We assume that these variations in the S distribution in the material might be due to a combination of different processes. In the case of Samples C and D, one possible explanation could be that the additional Se atoms deposited along with the NaF layer block the incorporation of S atoms into the bulk of the layer. Another possibility could be that the elemental diffusion from the surface is enhanced by the Na in the PD layer and in Samples C and D these diffusion channels could be occupied by the Se atoms deposited along with the NaF layer, thus the S atoms would gather at the surface. However, in order to understand the reasons of the differences on the element distribution it would be necessary to perform more specific experiments that allow the study of the elements diffusion into the material and the dynamic effects during the crystal growth.

Additionally, both EDX and GD-OES depth profiles, show that S is strongly concentrated near the surface region of the Reference sample without NaF layer. Similarly, we showed previously that Na plays an important role in the formation of the S-gradient and the [S]/([S] +[Se]) atomic ratio (de la Cueva et al. 2018). Elsewhere it has been reported that Na neutralizes the donor-like point defect V_{Se} in CIGSe solar cells (Kronik et al. 1998), increasing p-type conductivity and carrier concentration. Here and as it was observed by de la Cueva et al. (2018) and Ruiz-Perona et al. (2021), Na promotes the partial substitution of Se with S, replacing the possible Se vacancies by S, which increases the band gap energy of the kesterite material.

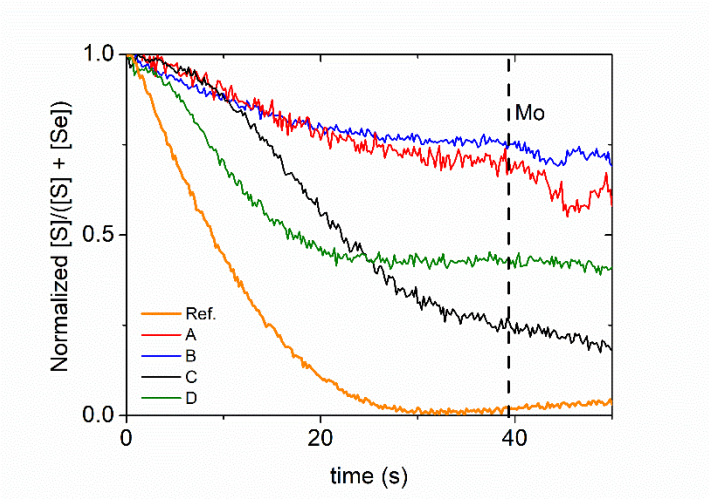

Fig. 3. GD-OES depth profiles of the normalized [S]/([S]+[Se]) atomic ratio for all the samples.

GIXRD diffractograms of all the samples at *GI* = 1º and 4º are plotted in Fig. 4. CZGSSe phases have been identified with its Bragg peaks located between CZGS (04-012-7580) and CZGSe (01-070-7623), which are also shown in Fig. 4. Mo Bragg peaks (04-014-7439) corresponding to the back contact have also been identified. Besides, there are two diffraction peaks located at around 15.1º and 57.4º that possibly belong to the $Cu_2Ge(S,Se)_3$ secondary phase. The Bragg peak at around 15.1º could also be assigned to $Ge(S,Se)_2$. In addition, the presence of the ZnS secondary phase with its main Bragg peak at 26.9º cannot be ruled out in case of the Reference sample when measured with GI angle of 1º.

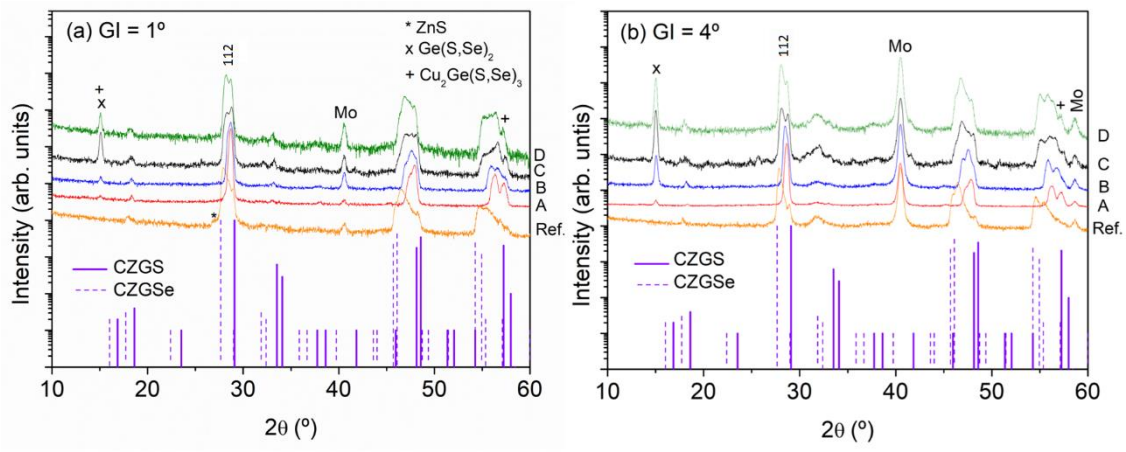

Fig. 4. GIXRD patterns measured at (a) *GI* = 1° and (b) 4º for Reference sample (orange), Samples A (red), B (blue), C (black) and D (green). The PDF data of $Cu_2ZnGeSe_4$ (dashed line), and Cu_2ZnGeS_4 (solid line), have been used for identification of the different phases.

Fig. 5 shows a more detailed plot of the 112 Bragg peak of CZGSSe for *GI* = 1º and 4º for each sample. A general shift towards higher diffraction angles in the *GI* = 1º curves compared to the *GI* = 4º can be observed, which denotes that the amount of S is higher at the surface. This is in good agreement with the previously discussed EDX and GD-OES measurements. Furthermore, the more uniform S distribution in Sample A can also be seen in Fig. 5. Unlike Sample A, Samples B, C, and D present a clear contribution of two different peaks related to the existence of two phases with different [S]/([S]+[Se]) atomic ratios. Also, in good agreement with the GD-OES results, a lower S concentration and a significant agglomeration of Se are observed in the bulk of the Reference sample, confirming the strong segregation of S near its surface.

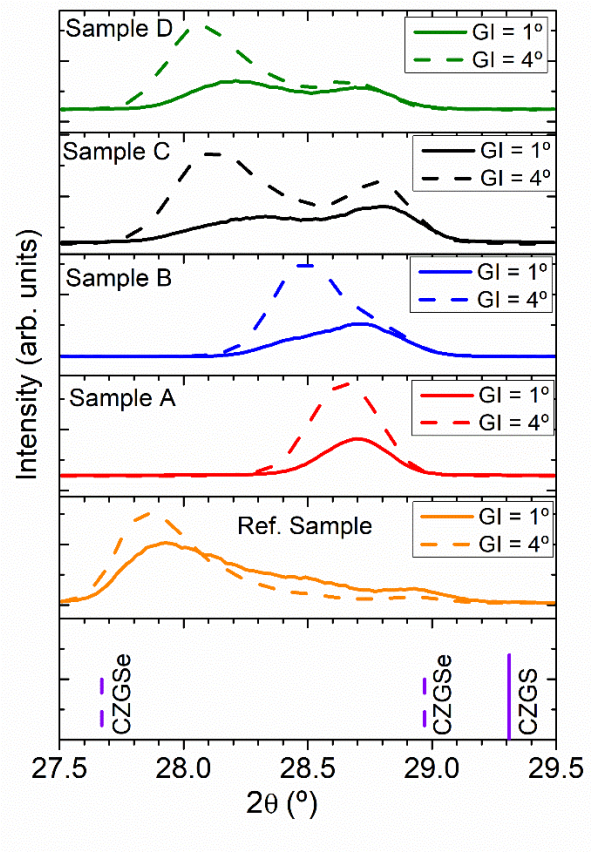

Fig. 5. 112 Bragg peak for all the samples investigated at *GI*= 1° (solid line) and *GI*= 4° (dashed line).

In order to identify all phases potentially forming at different depths of the CZGSSe layer, a multiwavelength Raman scattering analysis was performed. Due to the large bandgap energy of the samples, we used UV and visible excitation wavelengths (325, 442 and 532 nm) to obtain information mostly about the layer surface. Additionally, we used NIR excitation wavelength (785 nm) which penetrates the entire layer depth (except for the case of the reference sample in which the almost pure CZGSe phase at the back interface of the absorber layer limits the laser penetration depth). Independently of the used excitation wavelength, the spectra show a clear formation of S-Se solid solution of the CZGSSe phase (see Fig. 6) as can be concluded from the appearance of the Raman peaks related to the Se-Se vibrations (spectral range 160 – 215 cm^{-1}), S-S vibrations (spectral range 340 – 385 cm^{-1}), and S-Se vibrations (spectral range 215 – 255 cm^{-1}). Appearance

of the latter peaks is in agreement with the well-studied Sn containing CZTSSe compounds, where presence of new peaks related to S-Se vibrations was also observed (Dimitrievska et al. 2014), but less pronounced to the here discussed Ge containing solid solutions.

Analysis of the Raman spectra of the Reference sample measured under different excitation wavelengths confirmed that S was mainly segregated at the sample surface in the CZGSSe phase as well as in the ZnS secondary phase. The latter was clearly observed in the spectra measured under UV excitation, where the intensity of the peak related to the ZnS phase strongly exceeded the intensity of the peaks related to the kesterite phase (see Fig. 6.a.). Under the visible excitation wavelengths (442 and 532 nm), the intensity of the peaks related to S-S vibrations significantly exceed the ones related to Se-Se (see Fig. 6.b. and 6.c.), denoting the high concentration of the sulphur anions at the sample surface. This harshly changes when the NIR excitation wavelength (785 nm) is used, resulting in a spectrum with dominant Se-Se peaks (Fig. 6.d.), which corresponds to significant amount of selenium in the bulk of the absorber layer. Thus, a sharp gradient of the S distribution in the Reference sample can be confirmed, in agreement with EDX, GIXRD and GD-OES results.

In all samples with NaF, the Raman spectra measured under all excitation wavelengths are strongly changed compared to the Reference. In all samples, the presence of secondary phases like ZnS, ZnSe, $CuGeSe_2$, $CuGeS_2$, etc., as well as of Zn(S,Se) solid solutions can be excluded, as each of these phases is resonant to at least one of the applied excitation wavelengths and should therefore be clearly observable in at least one of the Raman spectra. However, next to the CZGSSe Raman peaks, there is a set of additional signatures found in the spectra that can be associated with the $Ge(S,Se)_2$ secondary phase, which was previously inferred from the XRD diffractograms of these samples. Since, according

to our knowledge, the crystalline phase of the $Ge(S,Se)_2$ solid solution was not yet studied by Raman spectroscopy in detail, a system of $Ge(S,Se)_2$ chalcogenide glasses with different [S]/[Se] ratio was analyzed, to provide reference values for this phase. In Fig. 6, violet bars indicate the position of the most intense peaks of the $GeS_{1.2}Se_{0.8}$ glasses at 208, 233, 262, 300, 350, 377 and 423 cm^{-1} (Han et al. 2014). These peaks overlap with the peaks of the main kesterite phase and therefore it is hard to unambiguously identify them in the spectra measured under any excitation wavelength. Nevertheless, appearance of a strong broad band close to 260 cm^{-1} can be interpreted as an indication of the presence of the $Ge(S,Se)_2$ secondary phase, for which several peaks related to different $Ge(S,Se)_2$ tetrahedral units vibrations are expected in this spectral range (Griffiths et al. 1983, Han et al. 2014) . The presence of this complex secondary phase as well as the strong overlap of its peaks with the main peaks of the CZGSSe phase hindered us determining the [S]/([S] + [Se]) ratio quantitatively in the kesterite phase. However, using the results of the multiwavelength Raman scattering study, the qualitative assessment of the changes in the in-depth gradient of the anions became possible. As mentioned above, the penetration depth of the 785 nm excitation laser is expected to be larger than the thickness of the CZGSSe layers, and this is confirmed by the appearance of $MoSe_2$-related Raman peaks in the measured spectra of all treated samples A-D (see Figure 6.d). Keeping in mind that $MoSe_2$ forms at the back side of the absorber layer, this denotes that under NIR excitation, the spectra contain the overall in-depth information of the whole layer. On the other hand, due to the low penetration depth of 532, 442 and 325 nm excitation lasers, the resulting spectra mainly contain information about the absorber surface. Taking this into account, it can be seen that the gradient of the [S]/([S] + [Se]) ratio is more pronounced in the Samples C and D, and is gentler in Samples A and B, which is in accordance with GD-OES and EDX measurements.

A comparison of the sulfur gradient in the Samples A to D with the Reference sample shows that post- and pre-deposition treatment of the absorber with NaF has a significant influence in the case of a further incorporation of the S by minimizing the gradient (observed in Samples A and B), while presence of Se vapors during the treatment allows a more precise control of the [S]/([S] + [Se]) ratio gradient (observed in the Samples C and D).

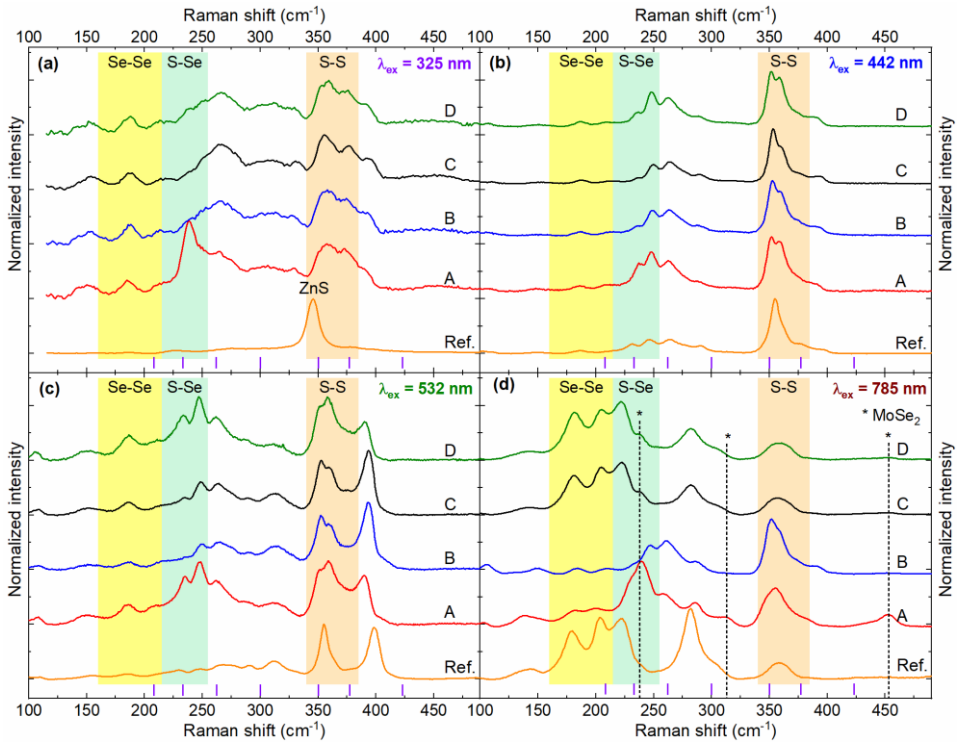

Fig. 6. Raman scattering spectra of the Reference sample and Samples A to D measured under (a) 325 nm, (b) 442 nm, (c) 532 nm and (d) 785 nm excitation wavelengths.

Fig. 7 shows cross-sectional (upper row) and top view (bottom row) SEM images of all the absorber layers investigated. Samples with NaF layers are characterized by a compact and columnar morphology without significant voids at the back interface, while in the Reference sample, without NaF, some voids at the back interface can be observed. Previous studies proved a correlation between the addition of Na to the kesterite and its

grain size, being larger as the Na content increases (Romanyuk et al. 2019). This is confirmed here, as a smaller grain size is also observed for the NaF free sample with lower Na content (see surface morphology). Additionally, Samples B and C present larger grains (> 1 μm) than Samples A and D. This could have a beneficial effect on the final device performance due to the reduced amount of grain boundaries, which can act as recombination centres. Nevertheless, it has been observed that larger grain size does not necessarily lead to higher efficiencies. As it can be observed in the surface images, there are apparent differences on the grain shape of Samples A-B and C-D. Whereas A and B present irregular shapes, Samples C and D have more regular and geometrical grains. Furthermore, the Reference sample presents a surface morphology more similar to those of Samples C and D, which could be related with the higher S concentration at the surface for those absorber layers. All the samples have a similar thickness, of about 1.3 μm.

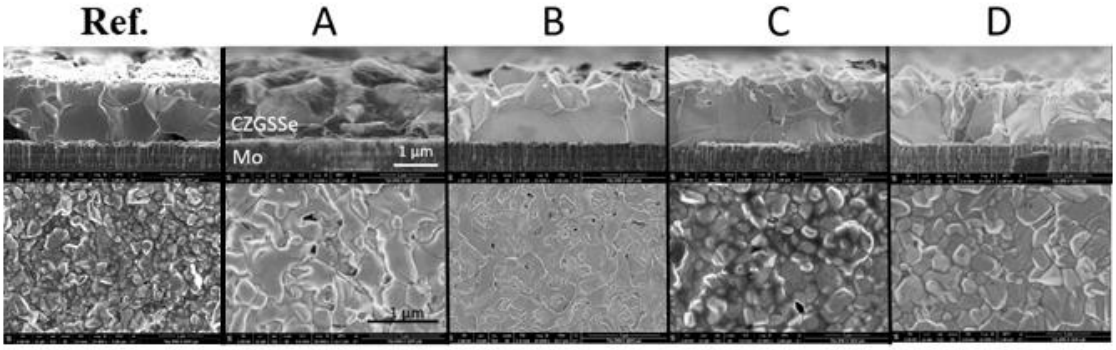

Fig. 7. Cross-sectional (upper row) and surface (bottom row) SEM images of CZGSSe/Mo structure for all the samples.

Photovoltaic devices with ITO/i-ZnO/CdS/CZGSSe/Mo/SLG structure were fabricated using these absorbers. *EQE* measurements of the best cells of each absorber are shown in Fig. 8 in solid lines along with the integrated J_{SC} in dashed lines. The *EQE* spectrum of the Reference sample is completely different from that of the samples with a NaF layer. The Reference sample is characterized by a lower spectral response from 350 to 600 nm

and absorption until 850 nm approximately presenting a much lower E_g than the other samples. Samples A through D mostly present similar *EQE* spectra with varying cut-offs of the absorption, indicating slightly different bandgap energies. Hereby, Sample B shows the lowest and Sample D the highest bandgap energy. Additionally, there is a significant difference between the spectra of Samples A-B and C-D at short wavelengths. Since the CdS buffer layer was deposited under the same conditions for all of the samples, these differences might be due to the different surface morphology and surface composition of the layers that was observed by SEM and GD-OES measurements respectively. These differences might have led to different growth conditions of the CdS resulting in a different CdS/CZGSSe heterojunction.

The optical band gap energy has been determined from the *EQE* measurements using the peak energy of the derivative of the *EQE* at longer wavelengths, and the values are shown in Fig. 9. The optical band gap energy of the Reference sample is about 1.63 eV. Samples A-D present much higher and similar E_g despite having significantly different sulphur content. Previous reports have shown that the band gap energy increases linearly with the sulphur content in the material (Guo et al. 2012), however, in these samples, EDX measurements show that the S content varies between 23 and 35 % in atomic weight ([S]/([S]+[Se] ~ 0.4 – 0.6) for Samples A-D. This is due to a more pronounced sulfur gradient in samples C and D compared to the almost uniform distribution of sulfur in the samples A and B. As shown in Fig. 9, it is clear that the samples where the NaF layer was deposited together with Se present a higher band gap energy than those where the NaF layer was deposited alone.

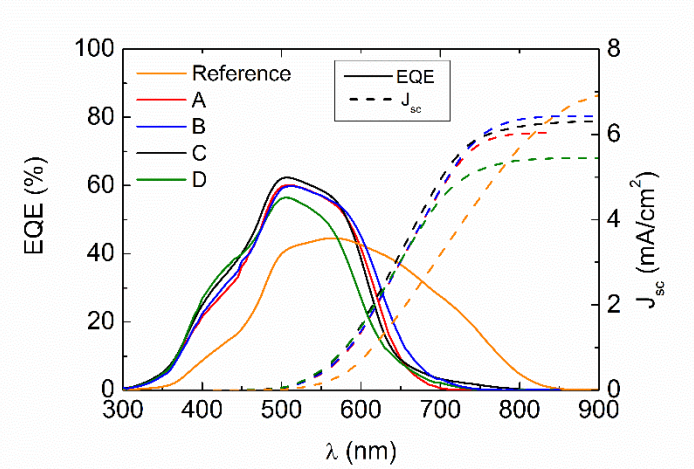

Fig. 8. *EQE* curves (solid line) and integrated J_{SC} (dashed line) for the best devices of each absorber layer.

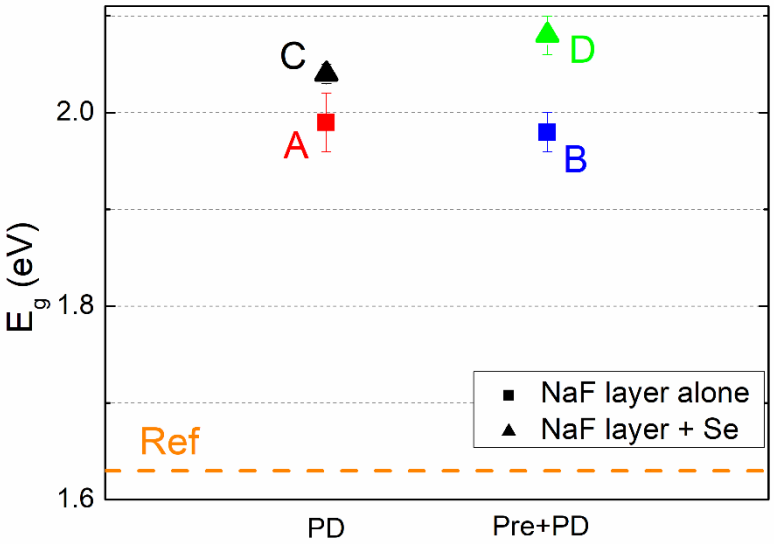

Fig. 9. Optical band gap energies calculated from the inflection point of the derivative of the EQE measurements at the long wavelenghts. Samples where the NaF layer was deposited in presence of Se are marked in triangle shape and samples where NaF was evaporated alone have square shape. Error bars were determined from the indetermination to assess the exact value from the inflection point of the EQE measurements at the long wavelength.

Table 2 shows the photovoltaic parameters V_{OC}, J_{SC}, *FF*, total area efficiency, shunt resistance R_{Sh} and series resistance R_S obtained from the *JV* curves and in parentheses the

values of J_{SC} and active area efficiency obtained from *EQE* measurements. Although variation between the J_{SC} values obtained from the *JV* curves and the integrated J_{SC} is observed, it does not seem to follow a trend. Since all samples were measured under the same conditions and they do not present significant differences in the structure, morphology or composition that can be linked to this, these differences could be attributed to the synthesis method and the presence of different kinds of barriers within the cell. While Devices B, C, and D have similar V_{OC} values, Device A presents a much lower V_{OC} compared to the other devices, accompanied by a very low shunt resistance. This might be related to the uniform bulk S distribution and a lower S concentration at the surface, as measured by GD-OES and Raman spectroscopy. This, in addition to the low values of J_{SC} and *FF*, lead to an efficiency of 1.1 % for Device A. Device B presents the highest J_{SC} value, reaching an efficiency of 3.2 %, the highest efficiency of the series. Devices C and D have lower values of J_{SC}, reaching efficiencies of 2.5 and 2.8 % respectively. The overall low short circuit current density values are due to the high band gap energies. A higher S content at the back contact could increase J_{SC}, since it could reduce recombination at the back interface (Yang et al. 2016).

These results denote the importance of having an optimal S gradient through the kesterite absorber, and the need of a higher S concentration at the front surface in order to increase the V_{OC}. On the other hand, the incorporation of a NaF layer before and after the evaporation of the CZGSSe leads to an enhanced J_{SC} and *FF* while keeping a high V_{OC}, above 815 mV. Moreover, Sample D presents the highest value of R_{Sh} and a much lower R_S compared to the other devices. The high series resistance of the solar cells could be the reason behind the low values of short circuit current density and *FF*. In addition, the presence of $Cu_2Ge(S,Se)_3$ ternary phase cannot be ruled out from GIXRD spectra. Khelifi et al. (2021) have shown a detrimental effect of Cu_2GeSe_3 phase on $Cu_2ZnGeSe_4$ solar

cells, which in principle could be a reason for the limited performance of the devices here, too. Moreover, the higher Cu content near the surface in most of the samples could be limiting the device performance because a Cu poor composition is desirable at the surface to enhance the CdS/CZGSSe interface (Chang et al. 2021). In the case of the Reference sample, the efficiency is limited to 2.2. %. Despite the lower sulphur content, a V_{OC} of 722 mV is achieved, much higher than that of Device A, which could be related to the higher S accumulation near the surface of its absorber layer. The presence of a significant amount of the ZnS secondary phase at the surface, as detected by Raman spectroscopy and GIXRD measurements, can be responsible for the limited device performance for the Reference sample as well (Ruiz-Perona et al. 2020a). Therefore, the main impact of Na on the absorber layer is the formation of a S-gradient through the kesterite film, which affects the optoelectronic properties of the corresponding PV device. These results manifest the promising future of this wide band gap material to be used for different applications, as for the fabrication of (semi)transparent solar cells. However, it is necessary to optimise the S-gradient through the absorber layer that allows for a simultaneous improvement of V_{OC} and J_{SC}.

Table 2. Photovoltaic parameters obtained from JV curves. J_{SC} and efficiency obtained from EQE measurements are shown in brackets.

Device	**V_{oc} (mV)**	**J_{sc} (mA/cm^2)**	**FF (%)**	**η (%)**	**Eg (eV)**	**R_{sh} (Ω/cm^2)**	**R_s (Ω/cm^2)**
Ref	722	7.1 (7.0)	44	2.2 (2.2)	1.63	207	11.85
A	382	5.8 (6.0)	49	1.1 (1.1)	1.99	466	12.37
B	817	7.5 (6.4)	51	3.2 (2.7)	1.98	546	14.05
C	854	5.9 (6.3)	50	2.5 (2.7)	2.04	680	15.75
D	821	6.2 (5.5)	55	2.8 (2.5)	2.08	747	5.76

4. Conclusions

Wide band gap kesterite thin film absorbers have been deposited by co-evaporation of CZGSe followed by a thermal treatment in presence of S and GeS. The effect of the Na content and the Na supply procedure on the compositional, structural, vibrational and morphological properties of CZGSSe absorber layers and corresponding photovoltaic devices has been investigated by varying the NaF layers configuration. The lower Na content, the lower sulphur incorporation and the stronger S-gradient through the absorber layer with a high S segregation at the surface was measured by EDX, GD-OES and Raman measurements. It was found that the elemental distribution depends on the Na addition process. The evaporation of Se together with NaF results in a strong [S]/([S] + [Se]) gradient through the CZGSSe layer and a different surface morphology. CZGSSe-based solar cells with band gap energies between 1.98 and 2.08 eV have been obtained when 15 nm NaF layer was added, presenting a slight increase in E_g for samples fabricated with Se-evaporation during the NaF deposition, which can be due to the higher S content on the surface of those samples. In contrast, the NaF free sample is characterized by a band gap energy of 1.63 eV, related to the lower S content. The devices with higher S content at the surface present high V_{OC} values (> 815 mV). These results show the importance of the S gradient through the sample. To the best of our knowledge, a record efficiency of 3.2 % has been achieved for CZGSSe-based photovoltaic devices with E_g of about 2 eV.

Acknowledgements

This work was supported by Spanish Ministry of Science, Innovation and Universities Project (WINCOST: ENE2016-80788-C5-2-R, CELL2WIN: PID2019-104372RB-C32) and European Project INFINITE-CELL (H2020-MSCA-RISE-2017-777968). MG acknowledges the financial support from Spanish Ministry of Science, Innovation and

Universities within the Juan de la Cierva Program (IJC2018-038199-I). Authors from IREC belong to the SEMS (Solar Energy Materials and Systems) Consolidated Research Group of the "Generalitat de Catalunya" (Ref. 2017 SGR 862). The authors acknowledge the service from the MiNa Laboratory at IMN-CSIC, and funding from CM (project S2018/NMT-4291 TEC2SPACE), MINECO (project CSIC13-4E-1794) and European Union (FEDER, FSE).

References

Becerril-Romero, I., Sylla, D., Placidi, M., Sánchez, Y., Andrade-Arvizu, J., Izquierdo-Roca, V., Guc, M., Pérez-Rodríguez, A., Grini, S., Vines, L., Pusay, B., Almache, R., Puigdollers, J., Pistor, P., Saucedo, E., Espíndola-Rodríguez, M., 2020. Transition-Metal Oxides for Kesterite Solar Cells Developed on Transparent Substrates, ACS Appl. Mater. Interfaces, 12,30, 33656–33669. https://doi.org/10.1021/acsami.0c06992.

Bremner, S.P., Levy, M.Y.,Honsberg, C.B., 2008. Analysis of tandem solar cell efficiencies under AM1.5G spectrum using a rapid flux calculation method, Prog. Photovolt. Res. Appl. 16, 225–233. DOI: 10.1002/pip.799

Caballero, R., Kaufmann, C. A., Rissom, T., Eicke, A., Manganiello, P., Schock, H. W., 2011. Evaluating different Na-incorporation methods for low temperature grown CIGSe thin-film on polyimide foils, Proceedings of the 37th IEEE Photovoltaic Specialist Conference, 000038-000037.

Caballero, R., Kaufmann, C. A., Efimova, V., Rissom, T., Hoffmann, V., Schock, H. W., 2013. Investigation of Cu(In,Ga)Se_2 thin-film formation during the multi-stage co-evaporation process, Prog. Photovolt: Res. Appl. 21, 30-46. https://doi.org/10.1002/pip.1233.

Cai, C-H., Wei, S-W., Huang, W-C., Hsu, C-H., Ho, W-H., Lai, C-H., 2017. Efficiency enhancement of $Cu_2ZnSn(S,Se)_4$ solar cells by S-modified surface layer, Sol. Energy Mater. Sol. Cells, 162, 21–29. https://doi.org/10.1016/j.solmat.2016.12.033.

Chang, X., Fu, J., Kou, D., Zhou, W., Zhou, Z., Yuan, S., Qi, Y., Zheng, Z., Wu, S., 2021. Synergistic incorporation of NaF and CsF PDT for high efficiency kesterite solar cells: unveiling of grain interior and grain boundary effects, J. Mater. Chem. A 9, 413-422. DOI: 10.1039/d0ta08224d.

Chirilá, A., Buecheler, S., Pianezzi, F., Blösch, P., Gretener, C., Uhl, A. R., Fella, C., Kranz, L., Perrenoud, J., Seyrling, S., Verma, R., Nishiwaki, S., Romanyuk, Y., Bilger, G., Tiwari, A. N., 2011. Highly efficient $Cu(In,Ga)Se_2$ solar cells grown on flexible polymer films, Nature Materials 10, 857-861. https://doi.org/10.1038/nmat3122

Choubrac, L., Bär, M., Kozina, X., Félix, R., Wilks, R. G., Brammertz, G., Levcenko, S., Arzel, L., Barreau, N., Harel, S., Meuris, M., Vermang, B., 2020. Sn Substitution by Ge: Strategies to Overcome the Open-Circuit Voltage Deficit of Kesterite Solar Cells, ACS Appl. Energy Mater., 3, 6, 5830–5839. https://doi.org/10.1021/acsaem.0c00763.

de la Cueva, L., Sánchez, Y., Calvo-Barrio, L., Oliva, F., Izquierdo-Roca, V., Khelifi, S., Bertram, T., Merino, J. M., León, M., Caballero, R., 2018. Sulfurization of co-evaporated $Cu_2ZnSnSe_4$ thin film solar cells: The role of Na, Sol. Energy Mater. Sol. Cells, 186, 115–123. https://doi.org/10.1016/j.solmat.2018.06.015.

Dimitrievska, M., Xie, H., Fairbrother, A., Fontané, X., Gurieva, G., Saucedo, E., Pérez-Rodríguez, A., Schorr, S., Izquierdo-Roca, V., 2014. Multiwavelength excitation Raman scattering of $Cu_2ZnSn(S_xSe_{1-x})_4$ $(0 \leq x \leq 1)$ polycrystalline thin films: Vibrational properties of sulfoselenide solid solutions, Applied Physics Letters 105, 031913. https://doi.org/10.1063/1.4891333.

Ford, G. M., Guo, Q., Agrawal, R., Hillhouse, H. W., 2011. Earth Abundant Element $Cu_2Zn(Sn_{1-x}Ge_x)S_4$ Nanocrystals for Tunable Band Gap Solar Cells: 6.8% Efficient Device Fabrication, Chem. Mater., 23, 10, 2626–2629, https://doi.org/10.1021/cm2002836.

Garcia-Llamas, E., Merino, J. M., Serna, R., Fontané, X., Victorov, I. A., Pérez-Rodríguez, A., León, M., Bodnar, I. V., Izquierdo-Roca, V., Caballero, R., 2016. Wide band-gap tuning $Cu_2ZnSn_{1-x}Ge_xS_4$ single crystals: Optical and vibrational properties, Sol. Energy Mater. Sol. Cells, 158, 147–153, https://doi.org/10.1016/j.solmat.2015.12.021.

Giraldo, S., Jehl, Z., Placidi, M., Izquierdo-Roca, V., Pérez-Rodríguez, A., Saucedo, E., 2019. Progress and Perspectives of Thin Film Kesterite Photovoltaic Technology: A Critical Review, Adv. Mater., 31, 16, 1806692. https://doi.org/10.1002/adma.201806692.

Green, M. A., Dunlop, E. D., Levi, D. H., Hohl-Ebinger, J., Yoshita, M., Ho-Baillie, A. W. Y., 2019. Solar cell efficiency tables (version 54), Prog. Photovolt. Res. Appl., 27, 7 565–575. https://doi.org/10.1002/pip.3171.

Griffiths, E., Espinosa, G. P., Phillips, J. C., Remeika, J. P., 1983. Raman spectra and a thermal laser annealing of $Ge(S_xSe_{1-x})_2$ glasses, Phys. Rev. B 28, 444-453. https://doi.org/10.1103/PhysRevB.28.4444

Guo, Q., Ford, G. M., Yang, W-C., Hages, C. J., Hillhouse, H. W., Agrawal, R., 2012. Enhancing the performance of CZTSSe solar cells with Ge alloying, Sol. Energy Mater. Sol. Cells, 105, 132–136 https://doi.org/10.1016/j.solmat.2012.05.039.

Han, X., Tao, H., Gong, L., Wang, X. Zhao, X., Yue, Y., 2014. Origin of the frequency shift of Raman scattering in chalcogenide glasses, Journal of Non-Crystalline Solids 391, 117–119. https://doi.org/10.1016/j.jnoncrysol.2014.03.021

Honsberg, C.B., Bowden S.G., 2020. Photovoltaics education website. https://www.pveducation.org/pvcdrom/tandem-cells

Khelifi, S., Brammertz, G., Choubrac, L., Batuk, M., Yang, S., Meuris, M., Barreau, N., Hadermann, J., Vrielinck, H., Poelman, D., Neyts, K., Vermang, B., Lauwaert, J., 2021.vThe path towards efficient wide band gap thin-film kesterite solar cells with transparent back contact for viable tandem application, Sol. Energy Mater. Sol. Cells 219, 110824. https://doi.org/10.1016/j.solmat.2020.110824.

Kim, S., Kim, K. M., Tampo, H., Shibata, H., Matsubara, K., Niki, S., 2016, Ge-incorporated $Cu_2ZnSnSe_4$ thin-film solar cells with efficiency greater than 10%, Sol. Energy Mater. Sol. Cells, 144, 488–492 https://doi.org/10.1016/j.solmat.2015.09.039.

Kodalle, T., Greiner, D., Brackmann, V., Prietzel, K., Scheu, A., Bertram, T., Reyes-Figueroa, P., Unold, T., Abou-Ras, D., Schaltmann, R., Kaufmann, C. A., Hoffmann, V., 2019. Glow discharge optical emission spectrometry for quantitative depth profiling of CIGS thin-films, J. Anal. At. Spectrom. 34, 1233-1241. https://doi.org/10.1039/C9JA00075E.

Kohl, T., Brammertz, G., Wild, J. de, Neuwrith, M. Meuris, M., Poortmans, J., Vermang, B., 2018. Fabrication of high band gap kesterite solar cell absorber materials for tandem applications, Thin Solid Films, 60, 247-252. https://doi.org/10.1016/j.tsf.2018.06.038.

Kronik, L., Cahen, D., Schock, H. W., 1998. Effects of sodium on polycrystalline Cu(In,GA)Se2 and its solar cell performance, Advanced Materials 10, 31-36.

Li, J. V., Kuciauskas, D., Young, M. R., Repins, I. L., 2013. Effects of sodium incorporation in Co-evaporated $Cu_2ZnSnSe_4$ thin-film solar cells, Appl. Phys. Lett., 102, 16, 163905. https://doi.org/10.1063/1.4802972.

Nakamura, M., Yamaguchi, K., Kimoto, Y., Yasaki, Y., Kato, T., Sugimoto, H., 2019. Cd-free Cu(In, Ga)(Se, S)$_2$ thin-film solar cell with a new world record efficacy of 23.35%, presented at the 46th IEEE PVSC, Chicago IL.

Neuschitzer, M., Espindola-Rodriguez, M., Guc, M., Marquez, J. A., Giraldo, S., Forbes, I., Perez-Rodriguez, A., Saucedo, E., 2018. Revealing the beneficial effects of Ge doping on $Cu_2ZnSnSe_4$ thin film solar cells, J. Mater. Chem. A, 6, 25, 11759–11772. https://doi.org/10.1039/C8TA02551G.

Niles, D. W., Al-Jassim, M., Ramanatahn, K., 1999. Direct observation of Na and O impurities at grain surfaces of CuInSe2 thin films, J. Vaccum Sci. Techn. A 17, 291-296. https://doi.org/10.1116/1.581583.

Rahmany, S., Etgar, L., 2020. Semitransparent perovskite solar cells, ACS Energy Lett. 5, 1519-1531. https://doi.org/10.1021/acsenergylett.0c00417.

Romanyuk, Y. E., Haass, S. G., Giraldo, S., Placidi, M., Tiwari, D., Fermin, D. J., Hao, X., Xin, H., Schnabel, T., Kauk-Kuusik, M., 2019. Doping and alloying of kesterites, J. Phys. Energy, 1, 4, 044004. https://doi.org/10.1088/2515-7655/ab23bc.

Ruiz-Perona, A., Sánchez, Y., Guc, M., Calvo-Barrio, L., Jawhari, T., Merino, J. M., León, M., Caballero, R., 2020a. Influence of Zn excess on compositional, structural and vibrational properties of $Cu_2ZnSn_{0.5}Ge_{0.5}Se_4$ thin films and their effect on solar cell efficiency, Solar Energy 199, 864-871. https://doi.org/10.1016/j.solener.2020.02.082.

Ruiz-Perona, A., 2020b. Efecto del Na sobre células solares de kesterita de banda prohibida ancha, Master Thesis, Universidad Autónoma de Madrid.

Ruiz-Perona, A., Gurieva, G., Sun, M., Kodalle, T., Sánchez, Y., Grossberg, M., Merino, J. M., Schorr, S., León, M., Caballero, R., 2021. Routes to develop a [S]/([S] + [Se]) gradient in wide band-gap Cu2ZnGe(S,Se)4 thin-film solar cells, J. Alloys Comp. 868, 159253. https://doi.org/10.1016/j.jallcom.2021.159253

Schnabel, T., Seboui, M., Ahlswede, E., 2017a. Band gap tuning of $Cu_2ZnGeS_xSe_{4-x}$ absorbers for thin-film solar cells, Energies 10, 1813. https://doi.org/10.3390/en10111813.

Schnabel, T., Seboui, M., Bauer, A., Choubrac, L., Arzel, L., Harel, S., Barreau, N., Ahlswede, E., 2017b. Evaluation of different buffer materials for solar cells with wide-gap $Cu_2ZnGeS_xSe_{4-x}$ absorbers, RSC Adv. 7, 40105-40110. https://doi.org/10.1039/c7ra06438a.

Son, D-H., Kim, S-H., Kim, S-Y., Kim, Y-I., Sim, J-H., Park, S-N., Jeon, D-H., Hwang, D-K., Sung, S-J., Kang, J-K., Yang, K-J., Kim, D-H., 2019. Effect of solid-H_2S gas reactions on CZTSSe thin film growth and photovoltaic properties of a 12.62% efficiency device, J. Mater. Chem. A, 7, 44, 25279–25289. https://doi.org/10.1039/C9TA08310C.

Vermang, B., Brammertz, G., Meuris, M., Schnabel, T., Ahlswede, E., Choubrac, L., Harel, S., Cardinaud, C., Arzel, L., Barreau, N., van Deelen, J., Bolt, P-J., Bras, P., Ren, Y., Jaremalm, E., Khelifi, S., Yang, S., Lauwaert, J., Batuk, M., Hadermann, J., Kozina, X., Handick, E., Hartmann, C., Gerlach, D., Matsuda, A., Ueda, S., Chikyow, T., Félix, R., Zhang, Y., Wilks, R. G., Bär, M., 2019. Wide band gap kesterite absorbers for thin film solar cells: potential and challenges for their deployment in tandem devices, Sustain. Energy Fuels, 3, 9, 2246–2259. https://doi.org/10.1039/C9SE00266A.

Wang, W., Winkler, M.T., Gunawan, O., Gokmen, T., Todorov, T. K., Zhu, Y., Mitzi, D. B., 2014. Device Characteristics of CZTSSe Thin-Film Solar Cells with 12.6% Efficiency, Adv. Energy Mater. 4, 7, 1301465. https://doi.org/10.1002/aenm.201301465.

Yang, K-J., Son, D-H., Sung, S-J., Sim, J-H., Kim, Y-I., Park, S-N., Jeon, D-H., Kim, J-S., Hwang, D-K., Jeon, C-W., Nam, D., Cheong, H., Kang, J-K., Kim, D-H., 2016. A band-gap-graded CZTSSe solar cell with 12.3% efficiency, J. Mater. Chem. A, 4, 26 10151–10158. https://doi.org/10.1039/C6TA01558A.